Article

The voltage-sensing domain of a hERG1 mutant is a cation-selective channel

Meruyert Kudaibergenova,[1] Jiqing Guo,[2] Hanif M. Khan,[1] James Lees-Miller,[2] Mahdi Mousaei,[1] Williams Miranda,[1] Van A. Ngo,[1] Sergei Yu Noskov,[1] D. Peter Tieleman,[1,*] and Henry J. Duff[2,*]

[1]Centre for Molecular Simulation and Department of Biological Sciences, University of Calgary, Calgary, AB, Canada and [2]Department of Cardiac Sciences, Libin Cardiovascular Institute of Alberta, University of Calgary, Calgary, AB, Canada

ABSTRACT A cationic leak current known as an "omega current" may arise from mutations of the first charged residue in the S4 of the voltage sensor domains of sodium and potassium voltage-gated channels. The voltage-sensing domains (VSDs) in these mutated channels act as pores allowing nonspecific passage of cations, such as Li^+, K^+, Cs^+, and guanidinium. Interestingly, no omega currents have been previously detected in the nonswapped voltage-gated potassium channels such as the human-*ether-a-go-go*-related (hERG1), hyperpolarization-activated cyclic nucleotide-gated, and *ether-a-go-go* channels. In this work, we discovered a novel omega current by mutating the first charged residue of the S4 of the hERG1, K525 to serine. To characterize this omega current, we used various probes, including the hERG1 pore domain blocker, dofetilide, to show that the omega current does not require cation flux via the canonical pore domain. In addition, the omega flux does not cross the conventional selectivity filter. We also show that the mutated channel (K525S hERG1) conducts guanidinium. These data are indicative of the formation of an omega current channel within the VSD. Using molecular dynamics simulations with replica-exchange umbrella sampling simulations of the wild-type hERG1 and the K525S hERG1, we explored the molecular underpinnings governing the cation flow in the VSD of the mutant. We also show that the wild-type hERG1 may form water crevices supported by the biophysical surface accessibility data. Overall, our multidisciplinary study demonstrates that the VSD of hERG1 may act as a cation-selective channel wherein a mutation of the first charged residue in the S4 generates an omega current. Our simulation uncovers the atomistic underpinning of this mechanism.

SIGNIFICANCE This multidisciplinary study combines experimental and computational efforts to discovers an omega current in recently cryo-EM resolved "nonswapped" topology voltage-gated potassium channels, the human-*ether-a-go-go*-related channel and resolves mechanisms behind the formation of the cation-selective conductance through VSD.

INTRODUCTION

The human-*ether-a-go-go*-related gene (hERG1), otherwise known as Kv11.1, encodes a voltage-gated potassium channel (1–3), which selectively conducts potassium ions in the heart and many other organs. The channel (4,5) governs the cardiac refractoriness due to its unique gating dynamics marked by very slow activation (4,6) and deactivation kinetics of over hundreds of milliseconds along with the very rapid voltage-dependent C-type inactivation (7,8). The fully functional form of the channel is assembled as a tetrameric protein made of four repeating α-subunits, each

have six transmembrane α-helical segments (S1-S6) with extracellular and intracellular domains (9,10). The transmembrane segments S1-S4 belong to the voltage-sensing domain (VSD) and S5-S6 segments make up the pore domain (PD) of the channel. These two domains are covalently linked by a short amino acid sequence, known as the S4-S5 linker. The VSD detects electrochemical potential differences across the membrane and transmits the energy via the S4-S5 linker to the PD. In response to the VSD, the PD either opens or closes, thereby regulating the flow of K^+ ions, denoted as the canonical current of the channel (11). Extracellular and intracellular domains of the hERG1, Per-Arnt-Sim and cyclic nucleotide binding domains, and a large intracellular S5-P-linker, a domain between the S5 segment and P-loop segments are also functionally involved in gating of the channel, a discussion of which is beyond the scope of this study.

The VSD generally adopts an hourglass shape with wide upper and lower vestibules exposed to the extracellular and intracellular milieu that meet at the narrow midpoint. The upper and the lower vestibules are separated by a hydrophobic plug, marked by a highly conserved aromatic residue, phenylalanine, which acts as a barrier preventing the free flow of water through the vestibules of the VSD. The hydrophobic plug also functions as the charge transfer center, allowing the positive charges of the S4 to slide across the charge transfer center. The S4 segment of the VSD is proposed to serve as a voltage sensor as the segment carries several positive charges including four basic arginine residues (R528, R531, R534, and R537) and two lysine residues (K525 and K538) spaced evenly on the helix (-^{522}GLLKTARLLRLVRVARK^{538}-), which jump from one binding residue to the next in response to the changes in transmembrane potential (12–15). Interestingly, most of the gating charge is thought to be transferred by only the first three charged residues K525, R528, and R531 in S4 (16). Although numerous biophysical data exist for the hERG1, the gating dynamics and kinetics have been notoriously difficult to understand and elucidate. For example, different mechanistic models have been proposed in attempts to explain VSD coupling with the membrane potential and the gate. Some works suggest extensive S4 motion during gating, while others report far less movement in the S4 suggesting a subtle voltage gating (17–21). The unique gating dynamics of the hERG1 and how S4 is coupled to the gate are also unclear. The availability of the hERG1 cryo-EM structure (~3.8 Å) in a depolarized voltage sensor and an open pore allows us to begin to scratch the surface of the VSD structure, function, and potentially the nature of its movement during the gating dynamics (22). At present, there appears to be no structure of the channel in its deactivated, closed, S4 downstate.

The open structure revealed a different packing topology than previously believed, as the VSD is directly packed to the PD with a very short S4-S5 linker, resulting in a "nonswapped" topology compared with *Shakers* (22). Loose packing of the VSD within itself and the tendency of S4 to be exposed to lipids is one of the striking features of the VSD in the hERG, hyperpolarization-activated cyclic nucleotide-gated (HCN), or *ether-a-go-go* (EAG) channels (23–26), which is supported by tryptophan scanning mutagenesis, as glycine substitutions in the S4 are more detrimental than of tryptophan (27).

In contrast to the hERG1 channel, the S4 in *Shakers* is presumed to be well shielded from the lipids by the intraprotein interactions with S1, S2, and S3 (28–30). The hydrophobicity of S4 was also found to be critical for gating in Kv11.1, suggesting that the tendency of the VSD to interact with the lipids in its relaxed open state is essential for the channel's relatively rapid gating dynamics (31). All these findings strongly suggest that the charged residues in the S4 may be exposed to lipids or water crevices within a membrane phase

or, alternatively, specifically interact with a lipid in at least one conformational state of the channel (27,32). A recent study exploring the packing of VSD and stability of salt bridges found in cryo-EM structure further endorsed the "loose" packing of key residues implicated in the gating charge transfer and showed persistent hydration of the VSD (32). The functional significance of either of the properties of hERG1 VSD is yet to be established. One plausible functional implication of having persistent hydration of VSD is the presence of nonconventional cation currents.

Previous studies (33) in *Shakers* established the crucial role of sensor hydration, but also emphasized an important functional role of the first charges in the sensor forming critical barriers for an ion passage across the membrane. Several mutations in the S4 and S2 of the VSDs have been identified to enable a novel ionic current with properties different from that of the α-current (canonical) of the PD, both in *Shakers* and sodium channels, Na$_v$1.2, Na$_v$1.4 (2,31,34). Those currents have been denoted as "omega" currents and are attributed to the flux of cations, such as K$^+$, Cs$^+$, and Li$^+$ through VSD (1,35). These omega currents can also be carried by guanidinium, protons, and other alkali ions (35). The phenomena of omega currents are not limited just to a peculiar biophysical property of various voltage-gated ion channels unlocked with the targeted mutagenesis. Familial mutations of ion channels that produce omega currents are implicated in human diseases, such as benign familial neonatal seizures and periodic paralyses (36,37). In *Shaker* channels, mutation of the first charged residue, R1, to a smaller hydrophobic amino acid along with a mutation of the adjacent subunit R2 is known to cause a cation leakage in the VSD of the channel when the S4 is at rest (2,3,35). In sodium voltage-gated channels Na$_v$1.4, a mutation of either outermost gating charges in a domain can induce a nonspecific cation conductance via VSD, disrupting the resting membrane potential and leading to normal and hypokalemic periodic paralysis in patients (2,38–42). However, it is important to note that the packing and orientation of the S4 in the VSD vastly differ between *Shakers* and the nonswapped topology voltage-gated channels, such as ERG, EAG, or HCN channels (23,24). Whether or not the VSD of the nonswapped topology proteins enables omega currents similar to that reported in other voltage-gated channels is yet to be established.

In this work, by mutating the K1 charge (K525) to serine, we discover a novel and sizable omega current in the K525S-hERG1 channel. We use a high-affinity hERG1 intracavity PD blocker, dofetilide, at high concentrations, to block the K$^+$ flux through the canonical pathway, to allow characterization of the omega currents stemming from ion flux through the VSD. We then further explore the conductance of the putative omega current using various charge carriers and protocols. The omega current of K525S shows characteristics of an omega current in the hERG1 VSD with many of the characteristics reported in studies of *Shakers* and Nav1.4 channels. Our simulations of open- and closed-state hERG1 show rapid

formation of water crevices and eventually stable omega currents in VSD subunits, the first element in the omega current formation in many other studied systems.

The replica-exchange molecular dynamics-umbrella sampling (REMD-US) calculations were used to understand key energetic component- and mutation-induced changes within the VSD that allow for the formation and propagation of the omega current. We find that K525 mutation to serine significantly reduces the energy barrier of the ion passing through the VSD and hence allows the formation of this omega current. The data show that the K525S-hERG1 mutant may conduct cations as large as guanidinium, thus likely adopting a dilated VSD configuration allowing hydration of the tunnel (32). This dilated state associated with the observed omega current was undetected by mutagenesis of K1 to other residues reported previously (19,27,43). Therefore, combined experimental and theoretical studies aimed at cross-examining the VSD structure of the hERG1 against biochemical and electrophysiology evidence suggest the formation of wide crevices within the VSD as a natural feature of this swapped-domain topology channel. Finally, our work highlights how the VSD of the hERG1 can be transformed into a cation-selective channel by reducing cation entry barriers and enhancing the local hydration of the sensor.

METHODS

Molecular biology

Methods for site-directed mutagenesis have been reported previously (44,45). Single- and double-mutant constructs of hERG1 were produced using conventional overlap PCR with primers synthesized by Sigma Genosys (Oakville, Ontario, Canada) and sequenced using Eurofins MWG Operon (Huntsville, AL). The hERG constructs were transfected into the human embryonic kidney 293 cells by the calcium phosphate method and cultured in Dulbecco's modified Eagle medium supplemented with 10% fetal bovine serum and 1% penicillin and streptomycin (Gibco DMEM (#11995) from Fisher Scientific, Pittsburgh, PA, USA).

Electrophysiology

The Tyrode extracellular solution contained 140 mM NaCl, 5.4 mM KCl, 1 mM $CaCl_2$, 1 mM $MgCl_2$, 5 mM HEPES, 5.5 mM glucose adjusted to pH 7.4 with NaOH. The 145 mM Cs^+, Li^+, and guanidine solutions were made by replacing all the extracellular Na^+ with an extracellular solution containing Cs^+, Li^+, and guanidine. Quinidine (30 μM final concentration) and dofetilide (2 μM final concentration) were dissolved in dimethyl sulfoxide (100–50 mM) and then diluted into experimental solutions before the experiments. The pipette solution contained the following: 10 mM KCl, 110 mM K-aspartate, 5 mM $MgCl_2$, 5 mM Na_2ATP, 10 mM EGTA (ethylene glycol-bis(-aminoethyl ether)-N,N,N,N-tetraacetic acid), 10 mM HEPES, and 1 mM $CaCl_2$. The solution was adjusted to pH 7.2 with KOH.

The conductance in control Tyrode solution was calculated as:

$$G = I / (V_{mem} − V_{rev}).$$

V_{mem} is the membrane potential. V_{rev} is the reversal potential of the current. In these experiments, measured average reversal potential of Tyrode solution is −18 mV. The relativity permeability ration (P_X/P_{K_+}) calculation was based on GHK equation:

$$V_{rev} = RT/zF \ln ((P_X[X]_o + P_K[K]_o) / (P_X[X]_i + P_K[K]_i)).$$

Where V_{rev} is reverse potential; P_X is the permeability of the channel to X ion and $[K]_i$ is the intracellular K^+ ion concentration. For the reversal potential measurement, the background conductance was electrically subtracted out of the currents at the same tail current potentials after a −90 mV hyperpolarization, in which no current was activated.

Statistical analysis of electrophysiology data

The software Statsview (Abacus Concepts, Berkeley, CA) or QTI plot (https://www.qtiplot.com/index.html), Grace (http://plasmagate.weizmann.ac.il/Grace/) were used to analyze the data. The null hypothesis of this study was used to compare the results observed in WT versus K525S hERG1. The null hypothesis was rejected when the *p* value was <0.05 as evaluated by an unpaired Student's *t*-test or a one-way analysis of variance with Tukey test if a multiway comparison was made. Paired data were recorded in the same cell with different cation replacements and a paired *t*-test was used. All variance measurements for electrophysiological data are shown as mean ± standard deviation (SD). The study was exploratory; before the start of the experiments there was no a priori reason to consider that one mutation would be different than another. In addition, we acknowledge that there may be other mutations that could be relevant. All the comparisons were prespecified, and all the comparisons are reported. The n values for each point of the concentration-response relationship are presented in the figure legends.

MD simulation setup

hERG1 depolarized VSD simulation

The hERG1-bilayer system was built using a cryo-EM structure (PDB: 5VA2) using a previously described protocol (46,47). The cryo-EM structure has missing loops, which were modeled using a three-step protocol: threading to generate initial models, low-resolution ROSETTA loop modeling, and high-resolution all-atom refinement and selection of models based on ROSETTA clustering (46). In brief, the channel was embedded in the explicit membrane consisting of phosphatidylcholine (POPC) lipids with water and ions (47). Force fields for lipids and protein were CHARMM36m, whereas a TIP3P force field was used for water molecules (48). The protein-membrane complex system was equilibrated for 250 ns and the simulations were produced for 3.5 μs. An Anton 2 built-in supercomputer from D.E. Shaw Research was used for the molecular dynamics (MD) production runs using Anton 2 software version 1.27.0 (49). The production runs were executed in a semiisotropic (NPaT) ensemble at a temperature of 313.15 K. The multiintegrator (multigrator) algorithm (50) developed inhouse by D.E. Shaw Research was used for temperature and semiisotropic pressure coupling (51). The time step for production runs was set to 2 fs and trajectories were saved every 240 ps. Nonbonded and long-range electrostatic interactions were evaluated every 2 and 6 fs, respectively. A 2.5 fs time step was used with nonbonded long-range interactions computed every 6 fs using the RESPA multiple time-step algorithm (52). Long-range electrostatics was calculated using the k-Gaussian Ewald method implemented to enhance performance on the Anton 2 platform (49,53) with a 64 × 64 × 64 Å grid. CHARMM36m force fields (48) were used to describe protein dynamics and CHARMM36 lipid parameters (54,55) were used to describe lipid membrane dynamics, for K^+ and $Cl^−$ ions, CHARMM-NBFIX LJ (56,57) were used along with a standard TIP3P water model. All simulations were carried out using the NAMD (v.2.12) package and visualized using VMD (v.1.9.4) and PyMOL (v.2.3) (58–60).

hERG1 hyperpolarized homology model simulation

The homology model of the closed-state hERG1 was constructed by combining two structures (spHCN and EAG) as these structures are

evolutionarily related to the hERG1. The Swiss-model program was used to build the closed-state homology model of the hERG1. The VSD of the hERG1 was based on the spHCN model (PDB: PDBDEV_00000032) with VSD down configuration. The PD was based on the EAG (PDB: 5K7L) closed structure (61–63). In PyMOL, two structures were aligned based on the alpha carbon backbone configuration of the open-state hERG1 (60). The tetrameric structure was also aligned based on the open state of the hERG1 structure (22) and the covalent bond between the VSD and the PD was created in PyMOL. Two variations of the closed structures were created that share the most difference in the S4-S5 linker (residues ∼545–550). The first variant includes residues 398–545 based on the VSD of the spHCN and residues 546–900 were based on EAG PD. The second variant includes residues 398–539 based on VSD of the spHCN and residues 540–900 based on EAG PD. Some residues in the structure clashed and were reoriented using PyMOL, which resulted in ∼10 different structures for each variant. Each structure was then embedded in the POPC membrane, containing 180 lipids in the upper and lower leaflets with water using Charmm-GUI (64). Each variant was minimized, equilibrated, and forwarded for a production run of ∼100 ns each using NAMD (58). After this, the VSDs were subjected to −250 mV to stabilize the hyperpolarized state of the sensor with a weak harmonic constraint (0.5 kcal/mol/Å^2) on S1, S2, and the S4-S5 linker (65,66). All other elements were allowed to fully relax.

Gating charge calculations

The gating charge was computed using an ensemble of 500 structures from the MD simulations for both the closed- and open-states of hERG1. Computation was performed using the Poisson-Boltzmann equation "coupling function" method from previous work (67,68). Only protein and lipids were used in the calculations, and all hydrogens in the membrane and extracellular loops were removed. The center of the bilayer was set to 0. Lipid charges were set to 0 and the resolution of the grid was set to 0.4 Å. Protein and lipid atoms were set to a dielectric constant of 2 and water was assigned a dielectric constant of 80. The ionic concentration was set to 150 mM. We used the PBEQ module of the CHARMM42b1 program to solve the Poisson-Boltzmann equation.

Steered MD and REMD simulations

The equilibrated structure of the VSD with all residues comprising helices S1 to S4 was extracted from production MD simulations of the depolarized hERG1. Using a CHARMM-GUI plugin, the VSDs of hERG1 and K525S hERG1 mutant (residues 398–539) were embedded in 148 POPC lipids with 16,000 water molecules and Cl^- and K^+ ions for neutralization (64). The K525S mutant was created using the CHARMM-GUI plugin membrane builder based on the equilibrated WT hERG1 system (69). For both systems, the initial simulation setup (Fig. S1, a and b) was minimized for 10,000 steps and subjected to the production run for MD simulation for 100 ns, according to the CHARMM-GUI protocol (64). Then the equilibrated VSD-membrane system was used in steered molecular dynamics (SMD) simulations to generate starting configurations for REMD simulations. A single K^+ ion was pulled along the z axis of the channel from −55 to +55 Å to cover the entire length of the VSD (−30 to 30 Å) and generate windows corresponding to the bulk region. The center of mass of the VSD was restrained during the SMD simulation. A pulling force of 5 kcal/mol/Å^2 with a speed of 10 Å/ns was used to propagate a single K^+ across the reaction coordinate described. The time step for all simulations was set to 1 fs/step, using the same simulation protocol as in the production MD runs.

Subsequently, the coordinates for REMD windows were extracted from the SMD simulation with 1 Å window spacing resulting in a total of 111 windows. The selection criteria for the replicas were based on the position

of a cation in each window: the cation had to be in the range of ± 0.25 Å from the center of each window for the REMD (70). Providing that the protein extent is from −30 to +30 Å, a 1D reaction coordinate for US simulations was chosen to range between −55 and +55 Å thus sampling ion permeation from the extracellular to intracellular solution. Z = 0 Å corresponds to the location of the hydrophobic constriction point located at the center of mass for two residues F463-I414 (Fig. 6). A flat-bottom harmonic potential of 12 Å in radius was applied to keep the permeating ion inside a cylinder, thus preventing other ions from entering the cylinder. The constraint protocol was recently tested with NAMD (v.2.12) (71) and was shown to reproduce constraint schemes previously used by Allen and Roux to study permeation in narrow channels (72). Each window was subjected to ∼27 ns of MD simulation using a harmonic restraining potential force constant of 3 kcal/mol/Å^2 and applied to the target, K^+. The first 13 ns is an equilibration while the last 14 ns were used for sampling calculations. Accordingly, the sampling time for each window is 14 ns. For error bars, sampling time was halved (14/2 = 7 ns) and the PMF was calculated for each half, and for overall simulation (14 ns). Then, the standard deviation was calculated using values from three parts and reported as the error bars for the entire PMF. The time step for all simulations was set to 1 fs/step, the temperature was kept constant at 310 K using Langevin dynamics, and the pressure was set to 1 atm with Nosé-Hoover Langevin piston pressure control using the MD protocol described previously (32). For each window, the position of the target ion was saved every 100 steps. The resulting distributions were used to calculate 1D PMFs using the weighted histogram analysis method (73). A brief overview of all simulations is shown in Table S1.

Analysis of the trajectories

Spatial locations of water molecules within the voltage sensor domain were identified by calculating (with the volmap tool in VMD) the density of water molecules on a 3D grid with a mesh of 0.3 Å. Then, Caver Analyst 2.0 was used to further analyze the size and shape of the tunnels formed in the VSD and the residues involved in the water tunnel formation (74). One hundred structures from each tetrameric chain of the hERG1 were analyzed for the presence of tunnels that correlated with the water tunnel formation. The structure that positively identified the water tunnel path was selected from each subunit for further analysis of bottleneck residues in Caver Analyst 2.0 (74,75). Caver Analyst 2.0 employs the algorithms from Caver 3.01, allowing visualization of the system (75). The starting point was defined by selecting the following residues: 470, 519, 531, and 534. Bottleneck radius was defined as 0.5 Å and clustering threshold was set to 5.0, shell depth 4.0, and shell radius was set to 3.0 Å. The same analysis was performed on the closed hERG1 VSD model and S466 hERG1 mutant. Water flow and permeation events within the VSD of each chain were calculated using custom in-house TCL scripts in VMD. All the molecular visualization figures were generated using PyMOL (v.2.3) (60).

Coordination number analysis of the REMD

The coordination number of K^+ to oxygen(s) was calculated by counting the number of oxygen(s) within the vicinity of 3.5 Å around the cation in each replica of the REMD simulations. We chose 3.5 Å as a cutoff value as it corresponds to the standard definition of the first layer of the hydration shell of K^+ (76).

We calculated the individual and total number of oxygen species found in the following chemical groups: carboxylate oxygen, carbonyl oxygen, water, and hydroxyl oxygen. The coordination number of each of these oxygen species found in the VSD tunnel of the water wire provides us with the structural information to compare the WT hERG1 and K525S hERG1 and the effects of K525 mutation on the permeation of the K^+ cation. The calculation of the solvent-accessible surface area was performed using an online tool, CASTp, where the extracellular solvent-accessible pocket of the VSD was detected using a spherical probe of 1.4 Å (77).

RESULTS AND DISCUSSIONS

K525X substitution opens a nonconventional permeation pathway in hERG1

Previous tryptophan scanning mutagenesis of S4 showed that the K525W mutant was well tolerated and marked an increase in the rates of activation and deactivation but had a minimal effect on the voltage dependence of the closed- to open-state equilibrium (27). Moreover, it was concluded that the VSD is loosely packed and some of the polar moieties are probably exposed to lipids (27). Mutation of K525 to a polar-uncharged residue, glutamine, was less tolerable than the tryptophan mutation resulting in significantly accelerated rates of activation (27). The K525Q mutation also activated at more hyperpolarized potentials and deactivated slower than the WT hERG1 (27). Mutation of the K525 to cysteine is generally reported to yield a less dramatic phenotype than the glutamine substitution and the channel is completely nonfunctional if K525 is mutated to alanine (19).

Since a number of K525X mutations have already been characterized, we decided to initially focus on the substitutions that would lead to a decrease in energy barriers for cationic entry compared with K1 (e.g., neutralizing basic residue), while still allowing for the interaction with lipid headgroups via hydrogen-bonding, potentially supporting the formation of the stable water crevice. Using this simple molecular logic, we made a choice for amphipathic substitutions (T, S, M) for the hERG1 mutagenesis, and we found that most of these constructs generated a substantial cation nonselective dofetilide-insensitive inward current elicited at hyperpolarized potentials. To confirm that the ion current is enabled via a nonconventional permeation pathway, experiments were executed in a solution containing a very high concentration of 2 μM dofetilide, a "gold standard" blocker of the intracavity (78). High concentrations of dofetilide ensure the block of a canonical permeation pathway, thus any current generated is likely to stem from an alternative, noncanonical pathway created or enhanced by the K1 mutation, namely K525S. The presence of dofetilide blocking the intracellular cavity allowed us to distinguish a dofetilide-sensitive current (Fig. 1 *a*) from a dofetilide-insensitive current—the current likely passing through a noncanonical pathway (Fig. 1, *a–d*).

The dofetilide-insensitive inward current is time dependent and voltage dependent, activated at hyperpolarized potentials. In review, the experimental results show the presence of a dofetilide-insensitive current that does not require ion permeation through the intramembrane cavity. This suggests that the origin of K525S hERG1 current could stem from ion
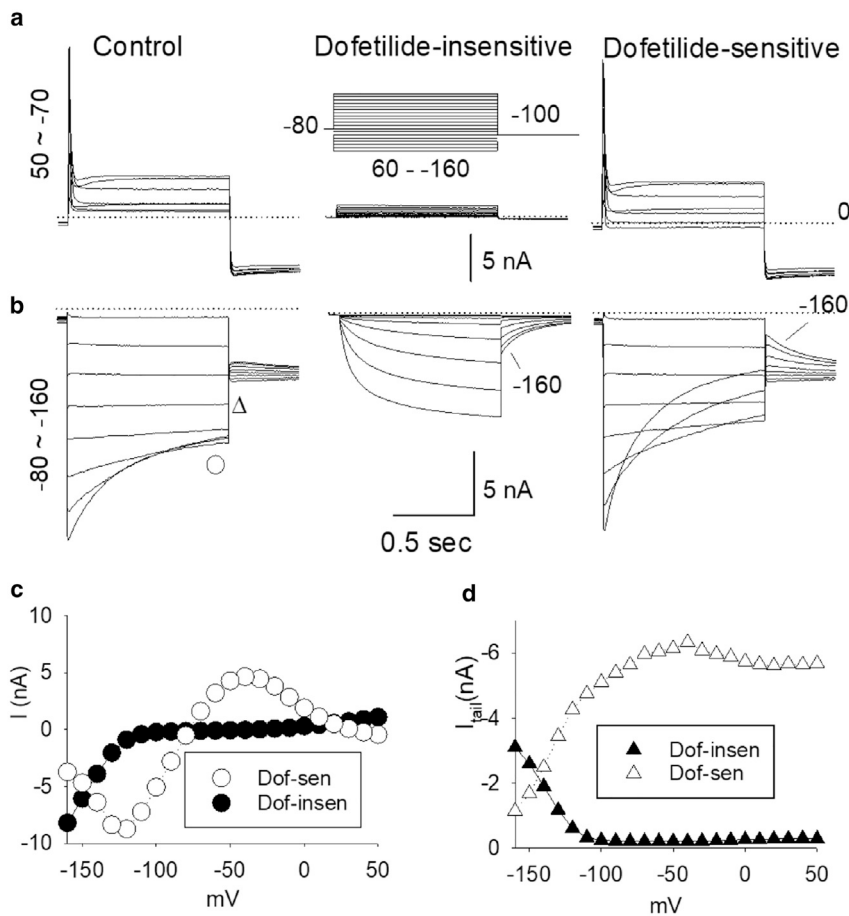

FIGURE 1 Traces of (*a*) depolarization- and (*b*) hyperpolarization-induced K525S currents in control and in 2 μM dofetilide (dofetilide insensitive). Dofetilide-sensitive currents are shown as a difference between measured currents in the presence of dofetilide and no-dofetilide control experiments. The experimental protocol is indicated in the inset of (*a*) and the potentials of test pulses are as marked on the left. (*c*) Semisteady-state current-voltage relationships, measured before the end of 1 s test pulses, of dofetilide-sensitive (dof-sen) and dofetilide-insensitive currents (dof-insen) of (*a* and *b*). (*d*) The tail current-voltage relationships of (*a* and *b*). The same characteristics are shown in all seven cells examined.

flux within the VSD, an omega current that had not been reported in nonswapped voltage-gated potassium channels.

We repeated our pharmacological blocking experiments using the same protocol, with divalent cations Ba^{2+} and another organic intracavity blocker, quinidine, to provide further evidence of the block of the canonical permeation pathway (Fig. S1). Ba^{2+} displays a relatively high affinity for the wild-type (WT) hERG1 (79), whereas quinidine is a less potent intracavity blocker (80) (Fig. S1). A similar drug-insensitive inward current was indeed detected in the presence of both Ba^{2+} and quinidine (Fig. S1). The same dofetilide-insensitive current was indeed detected in the presence of both Ba^{2+} and quinidine (Fig. S1). In contrast, a hERG agonist, NS1643, greatly blocked the omega current (Fig. S1). Incidentally, in our previous works, we proposed a binding site for NS1643 in the vicinity of L529, which is near the cytoplasmic mouth of the VSD (81). Thus, NS1643 could bind in the VSD vicinity and in its presence the noncanonical VSD conductance pathway may be blocked.

Next, we addressed whether the dofetilide-insensitive omega current required permeation through the canonical selectivity filter at the $_{626}GFG_{628}$ sequence. We created a double mutant, K525S/G628S, and used the single-mutant G628S as a control (Fig. 2). As can be observed, ion permeation through the canonical selectivity filter is ablated in the G628S channel. Even so, the hyperpolarization-activated omega current was still present in the double K525S/G628S mutant (Fig. 2). This confirms that omega currents observed in the K525S mutant are independent of flux through the intracavity PD and the canonical selectivity filter, suggesting that the cations flow through the VSD.

K525X enables formation of a large hydrated nonselective cation permeation pathway, omega current

Ion selectivity studies are shown in Fig. 3. The K525S hERG1 channel allows passage of monovalent cations
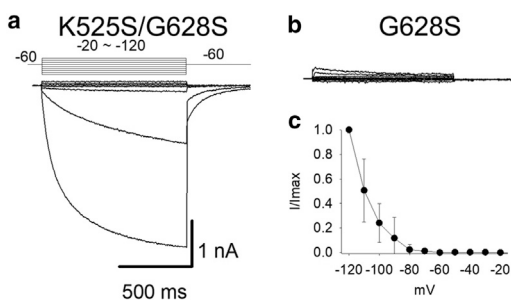
FIGURE 2 Ablation of the selectivity filter (G628S) deletes permeation through the canonic permeation pathway. Hyperpolarization-activated omega current remained in the double K525S/G628S mutant (a). Its single mutant G628S ablated the selectivity filter and completely deleted selective K+ current of hERG (b). The current traces of K525S/G628S (a) and G628S (b). Experimental protocol is in inset of (a). (c) Average tail conductance-voltage relationship of K525S/G628S. $N = 8$. mean $\pm$ SD were shown..
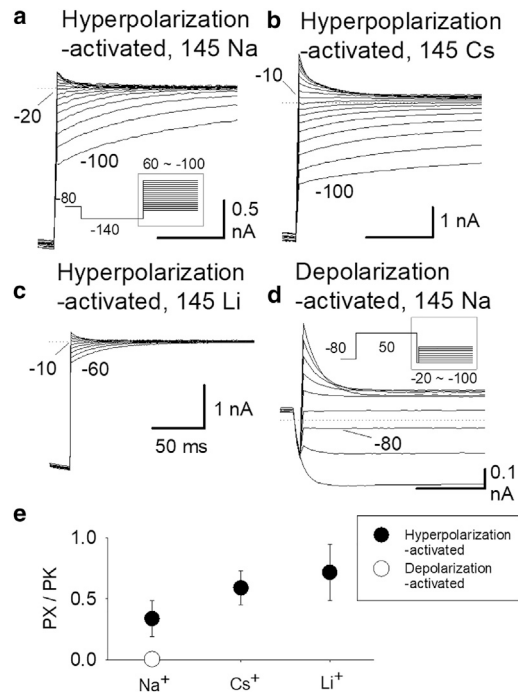
FIGURE 3 Ion selectivity of dofetilide-insensitive K525S current. The current trace families of reverse potentials of the dofetilide insensitive in control Tyrode solution (a), in 0 mM Na^+ and 145 mM Cs^+ (b), and in 0 mM Na^+ and 145 mM Li^+ solution (c) are shown. The experimental protocol is shown in the inset of (a). The current traces of reverse potential of conventional depolarization-activated current of K525S in control Tyrode solution are shown in (d). The experimental protocol in the inset of (d) was used. The relative ion selectivities of dofetilide-sensitive and dofetilide-insensitive current (Px/PK) of K525S channel on Na^+, Cs^+, and Li^+ are shown in (e), standard deviations are shown as bars.

(Li^+, Na^+, K^+, or Cs^+) (Fig. 3, a–c). The WT hERG1 selectivity filter is highly specific for the K^+ ions over Na^+ ($\sim$100:1) (5) and the gating of the channel may be modified by Co^{2+}, Ni^{2+}, Zn^{2+}, and Cs^{2+}. Fig. 3, a–c shows the reversal potentials of the K525S omega current in control Tyrode solution (containing 145 mM Na^+) (Fig. 3 a) and during replacement of extracellular Na^+ with Cs^+ (Fig. 3 b) and Li^+ (Fig. 3 c) with reversal potentials of around -20, -10, and -10 mV, respectively. The calculated permeability ratios (P_{X+}/P_{K+}) were 0.34 $\pm$ 0.14, 0.59 $\pm$ 0.14, and 0.71 $\pm$ 0.23 for Na^+, Cs^+, and Li^+ as charge carriers ($n = 8, 8, 6$) (Fig. 3 e). This indicates almost nonselective cation conductance. In contrast, reversal potentials of the depolarization activated current of K525S was around -80 mV, $P_{Na+}/P_{K+} = 0.0077 \pm 0.0023$ ($n = 4$) (Fig. 1 d), consistent with a K^+ selective current which was the same as WT hERG1. The loss of cation specificity of the omega current of the K525X channel is also consistent with the idea that the canonical selectivity filter (GFG) is not part of the permeation pathway for the dofetilide-insensitive K525S omega inward current. In review, these data indicate that the inward omega current consists of a nonselective cation conductance.

Some omega current pathways allow guanidinium to permeate the noncanonical permeation pathway as observed in the Nav1.4, *Shakers*, and Kv3 (35,82,83). Accordingly, we assessed whether the noncanonical current observed with the double mutation K525S/G628SA allowed permeation with the larger organic guanidinium cation for the hERG1. In contrast, WT hERG1 does not conduct guanidinium. Fig. 4 shows that both Na$^+$ and guanidine$^+$ are readily permeable across the VSD of the K525S alternative pathway.

We created a range of substitutions (K525X) to assess whether the omega current was dependent on the amino acid substituted at the K525 site (Fig. 5). Most amphipathic substitutions yielded similar hyperpolarization-induced phenotypes. These data highlight the importance of the location of the charged residue (K1) rather than the exact chemistry of the side-chain group (Fig. 5).

Overall, our experimental results indicate the K525X mutants result in a new permeation pathway in the VSD resulting in omega current. hERG1 VSD is structurally and mechanically completely different in comparison with the nonswapped channels. One may expect the presence of omega current under depolarized potentials during the mutation of the lower part of the VSD, namely R531 and R534, similarly to the observations in Nav1.2a and Nav1.4 (2,38). Our results indicate that hERG1 is not analogous to previous studies as there was an absence of any leak currents with R531E and R534Q mutations (Fig. S2). To provide a molecular understanding of the reduced barrier for cation flow through the nonswapped VSD, we explore the energetic underpinning of the permeation pathway utilizing molecular simulations.
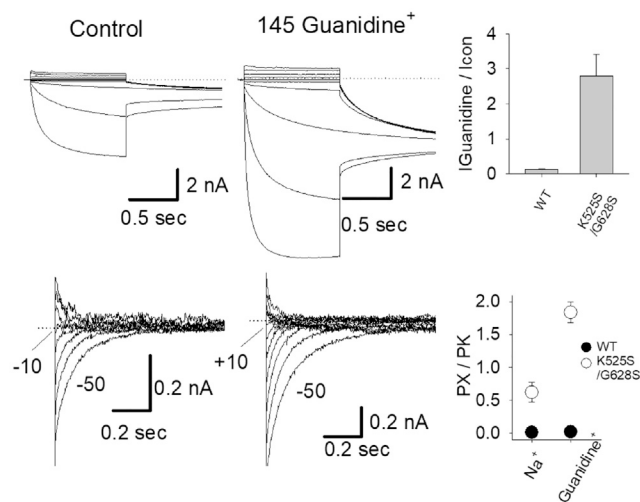

FIGURE 5 (*a*) Hyperpolarization-activated dofetilide-insensitive current components of various K525 mutations. The currents were induced by -140 mV hyperpolarization in 2 mM dofetilide. (*b*) The average amplitudes of K525X mutations. $N = 4$, 10, 16, 5, 8, 5, 5, 5, 7, 8, and 5 for K525A, C, G, H, K, M, N, Q, R, S, and T, standard deviations are shown as bars.

FIGURE 4 Current traces of K525S/G628S in the test protocols of activation (*a*) and reversal potentials (*b*), in control and guanidinium+ (Gua$^+$) solutions. Guanidine solution-induced changes in current amplitude (*c*) ($n = 3$, 3 in WT and K525S/G628S) and channel selectivity of K525S/G628S (*d*) ($n = 3$, 4 in WT and K525S/G628S) were plotted in comparison with WT hERG1. The same experiment protocols used as in the previous figure, standard deviations are shown as bars.
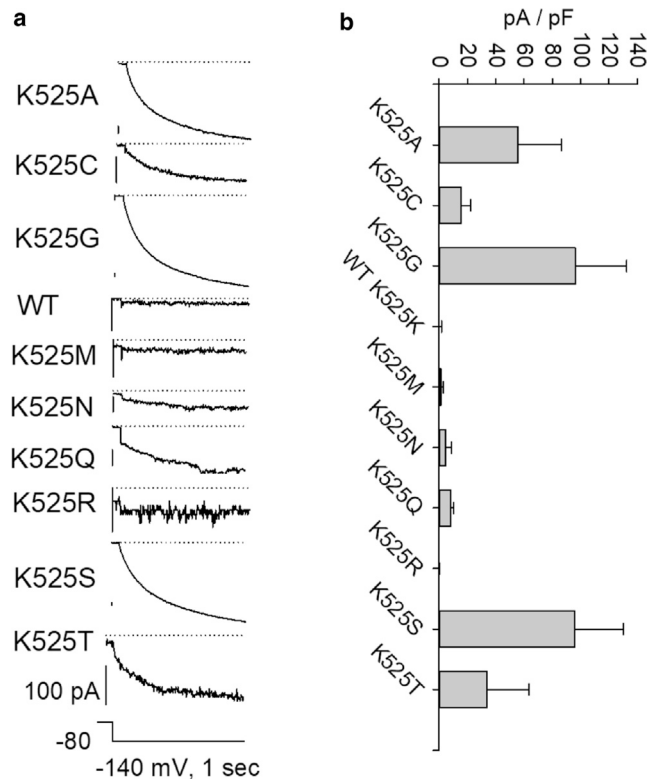
Closed- and open-state hERG1 VSD is loosely packed with wide-open crevices

The unbiased 3.2 μs long MD simulation of the depolarized WT hERG1 shows that the VSD of the channel forms wide crevices in the VSDs allowing slow leakage of water (Fig. S3, *a* and *b*). Next, we used Caver Analyst 2.0 to characterize the width of the tunnels and the network of residues contributing to the formation of this leaky water gate (74). Key residues forming the narrowest confinement in the tunnel are R534, R537, D501, D466, L538, and F463 (Table 1). Formation of the hydrated crevices in VSD as the channel relaxes is not destabilizing salt bridges shown to be crucial for the open state and they are consistently present in the simulation (Fig. S3 *a*). These salt bridges are in excellent agreement with the general results of previous experiments mapping out key salt bridges located near the VSD confinement (Fig. S3 *a* and Table S3). For example, D509 was reported to interact with R528 ($\sim$94.9% average occupancy, Table S3) (84) and D460, crucial for the activation and stabilization of the open state (85).

Moreover, it has been reported that R531, D456, D460, and D509 are coupled during the activation with D411 and D466, paralleling our salt bridge analysis of the WT

TABLE 1 Results from Caver Analyst 2.0, characterizing water tunnels formed within the voltage-sensing domains of the closed-state hERG1, the S525 closed-state hERG1 and WT hERG1 from the snapshots of the molecular dynamic simulation

hERG1	Bottleneck radius (Å)	Length of the tunnel (Å)	Curvature of the tunnel (Å)	Average throughput	Key residues
Closed hERG1	1.02	22.76	1.18	0.201	K407, N470, R537
S525 closed hERG1	1.47	23.59	1.23	0.250	I414, D466, R534
Open hERG1[a]	0.72[a]	28.15[a]	6.48[a]	0.241[a]	R534, D466, F463

[a]Values for the open-state hERG1 are the averages of four values from four chains, see Table S2 for a detailed breakdown.

depolarized hERG, which reveals complex and cooperative ionic pairing interactions (Fig. S3 and Table S3) (86). In simulation, D466 may interact with K538 directly (~80.5% average occupancy) and R534, but does not directly come in contact with R531 (0% occupancy rate). D466 interaction with K538 may also be affected by neighboring salt bridges, such as the interaction dynamics of neighboring D411 with K538 (~86% average occupancy rate) (Fig. S3). There is a complex interplay between several salt bridges in the VSD. Accessibility studies have also reported a salt bridge, D460-D509, involved in stabilizing one of the open states of the channel, which is not observed in our simulation (87). However, R528 seems to reside between D460 and D509, potentially affecting the dynamic salt bridge between D460 and D509 predicted in the experiments (87) (Fig. S3). D509 is known to stabilize the relaxed state of the VSD of the hERG1 as mutation of D509 results in loss of hysteresis and accelerated deactivation (88). D509 forms salt bridges with R528 (>90% occupancy, Table S3) and may interact with K525 (~25% average occupancy rate, Table S3 and Fig. S3). D456 is reported to form stable interactions with R528 (~77% average occupancy rate, Table S3) and R531 (~25.9% average occupancy rate, Table S3) (19,20); D460-R531 interactions are observed ~89% of the time (Table S3), which is reported in the literature, stabilizing the open state (86) (Fig. S3 a). The salt bridge interactions in the VSD are complex and involve several breaking and reforming of salt bridges throughout the simulation. Moreover, the presence or stability of salt bridges may be affected by the distant interatomic interactions within the VSD. Thus, apart from calculating the salt bridge occupancy, it is important to qualitatively and visually assess the dynamics within the VSD (Fig. S3).

Accessibility tests using extracellular reagents indicate the presence of a water-filled crevice that penetrates deep within the voltage sensor domains of the hERG1 near the cytoplasmic halves of S1 and S2 transmembrane domains with confinement at or near D460 (S2), D509 (S3), D466, and D501 (Fig. S3, a and b) (20,87,89). The residues forming the confinement in MD simulations include R534, F463, and D466 (Table 1). Therefore, hydrated VSD structures inferred from microseconds-long MD simulations are in general agreement with previous works of surface accessibility data that indicated the loose VSD packing and wide crevices present in the VSD (20,27,43,87,89,90). Positions 522-529 are readily accessible to water in our simulation reflecting the experimental accessibility data of pCMBS application

on resting state hERG (90). Moreover, metal ions, such as Cd^{2+}, are also predicted to bind and access the region around D509, D460, and D456 implying easy accessibility to those sites (91). The percent water distribution along the z axis of the voltage sensor shows that the least amount of water molecules is within the hydrophobic restriction point, around F463-I414 (Fig. S3 c).

Our molecular dynamic simulations clearly show that, in the open state, depolarized VSD of the hERG is loosely packed and forms a thin water tunnel (Fig. S3). This may provide some evidence of the potential conductance of ions through the VSD and elucidates numerous biophysical data indicating large water cavities within the VSD of the hERG1. Our experimental results for omega current, however, were obtained for the hyperpolarized, closed-state hERG1. For comparison, we built a closed-state hyperpolarized model for the hERG1 and K525S mutant based on recently published work on its molecular cousins, spHCN and EAG (61,62). The closed-state model was validated by calculating the gating charge (~1.4e/subunit) and by comparing this with existing biophysical experimental data. Using the same protocols as for the open-state hERG1, we analyzed tunnels using Caver 2.0 Analyst for both the hyperpolarized hERG1 and the S525 mutant (Table 1). The S525 mutant forms a wider water tunnel (1.47 Å) than in the closed hERG1 state (1.02 Å) (Table 1 and Fig. 6). Bottleneck residues for the S525 mutant are I414, D466, and R534, whereas for the closed-state hERG1 bottleneck residues are K407, N470, and R537 (Table 1). Both open and closed states of hERG1 yielded similar water cavities and both structures were the most constricted at the hydrophobic plug, F463 (Fig. 6).

Analysis of salt bridges within the VSD shows that the loss of K525 has a downstream impact on the VSD stability as the topology of salt bridges changes completely (Fig. 7 and Table S3). In the hyperpolarized VSD of hERG1, K525 is stabilized by interactions with D460 with 97% occupancy, which essentially allows K525 to act as a "gatekeeper" of the VSD tunnel (Table S3). Mutation to site 525 disrupts major salt bridges and even causes the formation of new salt bridges, such as D501-R531 (93.38% occupancy in the K525S mutant and 0% with WT hyperpolarized hERG1) (Fig. 7 and Table S3). The hyperpolarized, closed-state hERG1 model forms salt bridges predicted by the experiments. The D411-K407 salt bridge is predicted to form in the closed-state hERG and contributes in slow activation of the channel. Our simulations show a D411-K407 occupancy
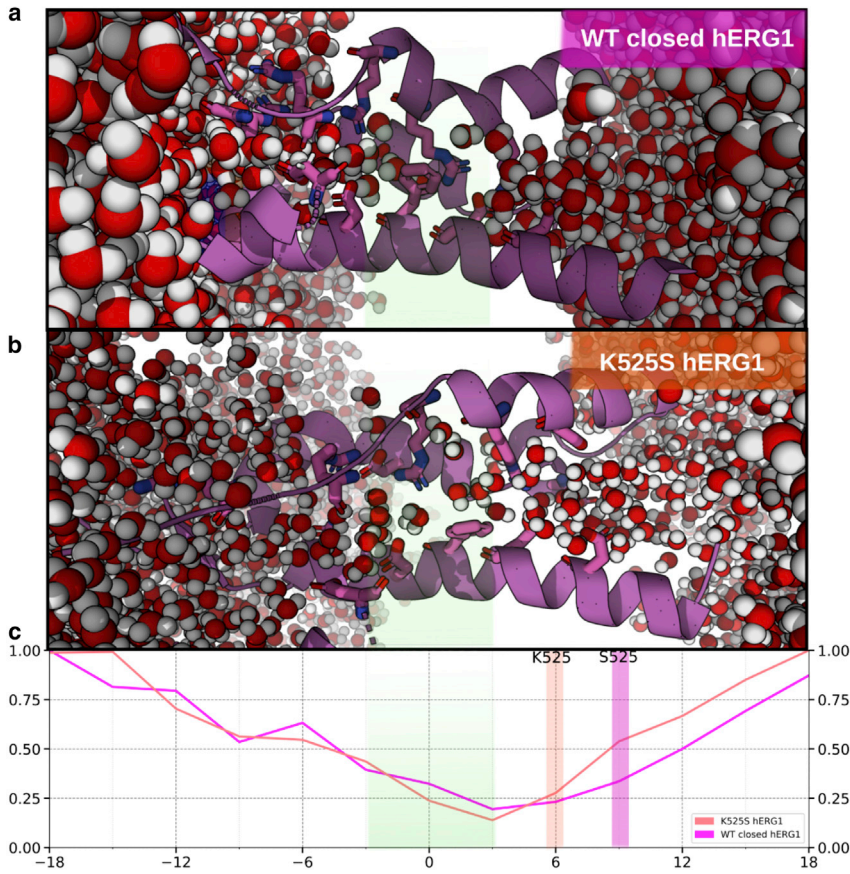
FIGURE 6 Cartoon representation of the closed-state VSD of (*a*) hERG1 and (*b*) K525S closed-state hERG1 with water wires in the VSD. A portion of the S1 was omitted for clarity and other relevant residues are shown as sticks and labeled accordingly. (*b*) General organization of the water wire present in the hyperpolarized WT hERG1 VSD model and the K525S-hyperpolarized hERG1, both aligned along the *z* axis. (*c*) Average fraction of water molecules inside the VSD relative to the bulk (set to 1) along the *z* axis; purple corresponds to the WT closed hERG1 and salmon corresponds to K525S hERG1. The area shaded in light green corresponds to the location of the hydrophobic plug (F463-I414). To see this figure in color, go online.

percentage of 88.55% for the WT hERG1 and 99.97% for the K525S mutant (Table S3). D456-K525 (20) occurs ~16% of the time, whereas D411-K538 (92) interactions also reported in stabilizing the closed state have an occupancy rate of

~76.73%. MTSET experiments reveal that D466 is more accessible in the closed state than the open state (16). Our simulations seem to parallel these results, as D466 forms far fewer salt bridges in the hyperpolarized state compared

WT hERG1 closed state	
D411-K407	88.55
D460-R528	88.31
D460-K**525**	96.98
E518-K434	97.16
E519-K434	95.16

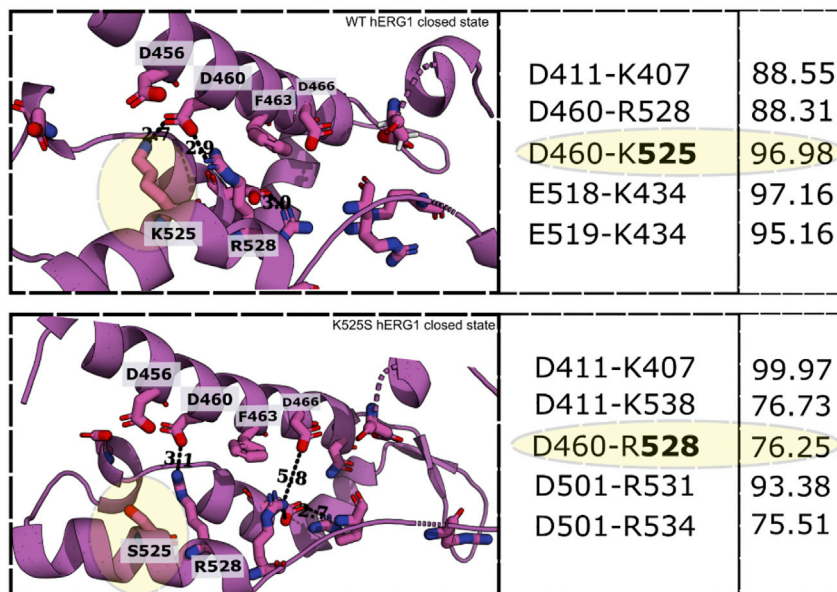| K525S hERG1 closed state	
D411-K407	99.97
D411-K538	76.73
D460-R**528**	76.25
D501-R531	93.38
D501-R534	75.51

FIGURE 7 Mutation at site 525 changes the network of salt bridges within the VSD contributing to the formation of a wider water tunnel. On the left panel, the VSD is represented as a purple cartoon, showing a top down perspective of the VSD, and relevant residues are shown as sticks and labeled accordingly. Distances between residues are shown as dashed lines. The middle panels are the major salt bridges present within the simulation for two modes, and the far-right panel corresponds to the percent occupancy. Highlighted in yellow is a site corresponding to 525. To see this figure in color, go online.

with the depolarized state (D466-K538 and D466-R534, Table S3) and forms wider water tunnels. D411-K538 interactions are predicted to form salt bridges during early closed state or intermediate transitioning states, thereby limiting the barrier of activation speed (92). The D411-K538 salt bridge is not observed in our closed model but in the depolarized state instead (Table S3). D466 and D501 are heavily involved in several salt bridges in the depolarized state, as discussed earlier (Table S3) and supported by experiments (87), the interactions of which are disrupted or completely absent in the hyperpolarized models. K525 in the hyperpolarized model forms a salt bridge with D460 with an occupancy rate of 96.98%, and located in close proximity to D456, thereby stabilizing the gate of VSD (Fig. 7 and Table S3). The interaction is absent in the depolarized WT hERg (~0%, Table S3). R528 is also shown to interact with D460 (~88.3% occupancy rate), which may further stabilize the region, although the same interaction is observed in the depolarized WT hERG1 (Fig. 7 and Table S3). When the K525 is mutated to S525, the salt bridge between D460-K525 is lost, thus D460 interacts only with one other charge, R528 (D460-R528, 76.25% occupancy rate). The mutation results in further changes in the fine intermolecular interaction within the VSD (Table S3). Although there are some fine differences in salt bridges formed within the depolarized and hyperpolarized models, overall structurally two states are similar with RMSD values between 2 and 3 Å, and similar water tunnels and constriction points (Figs. S3, S5, and S6).

The experiments show omega current only for the closed-state VSD of the hERG1, whereas the pulling of K^+ ions through the VSD were simulated on the depolarized hERG1. Given that structurally these states were similar, we wanted to ensure a stable VSD like the one in the WT hERG1 instead of a homology model. The stability and similarity of the VSD of both states is reflected by their similar RMSD values, ranging between 2 and 3 Å when α-carbonyl backbone atoms of the VSD (S1-S4) are aligned, and a very similar water tunnel formed within the channels (Figs. S5 and S6). Therefore, results from PMF of depolarized hERG may provide a biophysical explanation how the omega current may form within the VSD of the hyperpolarized hERG. Until the structure of the closed state, hyperpolarized VSD hERG1 becomes available, utilizing available experimental data may be the only option to understand the key forces causing the phenomena.

The K525X mutation decreases the energy barrier of the cation at the hydrophobic plug of the channel

Next, we studied the energetics of K^+ conduction through the VSD of the WT hERG1 and the K525S using the REMD-US method by computing 1D-PMF profiles of an ion traversing the VSD. The molecular representation of the simulation system is shown in Fig. S4 a. The resulting

PMFs for WT and a mutant are shown in Fig. 8 a; the PMF covers pathways of the ion in the aqueous space between Z = −55 Å and Z = 55 Å; with a reaction coordinate 0 Å corresponding to the location of the hydrophobic constriction point located at the center of mass of two residues F463-I414. The 1D-PMF profile shows that the WT hERG1 and the mutant have the highest energetic barrier at the narrowest hydrophobic restriction site of the VSD, F463-I414 (Fig. 8 a). F463's role as a potential hydrophobic plug in hERG1 has been largely based on the comparison with F290 of *Shakers* (43,65,93). Our simulations provide direct structural evidence for the role previously ascribed to F463. It is part of the hydrophobic gate in the VSD domain of the hERG1 channel, but the simulations suggest that this gate is leaky. The mutation widens the hydrophobic constriction point at F463, denoted as a reaction coordinate 0 in Fig. 8 a, thereby allowing more water molecules to traverse through the VSD even forming a transient pore (Fig. 8 a). The abundant presence of water molecules in the mutant allows potassium ions to remain partially hydrated, even at the hydrophobic constriction (Fig. 8 b). This partial hydration of permeating cations lowers the energetic cost of traversing through the VSD (Fig. 8 a), including the region near the hydrophobic constriction. This finding is in contrast to the proposed tightly packed hydrophobic gate in *Shaker* channels (65). The hydrophobic gate (F463-I414) in hERG VSD does not completely constrict the flow of water. This observation from MD simulations lends structural support to the reported data on divalent cations binding to the VSD of the hERG1 around D501, e.g., residues in the vicinity of hydrophobic confinement (87). The deep penetrations of divalent cations into the VSD-like domains have also been reported for the voltage-gated proton channels, where the formation of the water wire is an essential step in the permeation mechanism (94,95). The K525S VSD domain allows for partial cation hydration across an entire permeation pathway. The observed partial hydration of the cation across the entire permeation pathway in K525S-hERG (Fig. 8 b) explains the decrease of the barrier at the hydrophobic constriction by 7.5 kcal/mol relative to the WT hERG1 (Fig. 8 a). The important role of water in reducing the permeation barrier for cations has been firmly established in many other ion channels (96).

An additional factor that contributes to the observed omega current is related to the impact of the mutation on the cation entry site, at 525 (Fig. S4). The charge neutralization at K525 evidently disrupts interactions in the immediate vicinity of the potassium entrance point (Z ~8 Å). The S525 preferentially interacts with the surrounding lipids, while K525 predominantly interacts with other residues in the VSD (Fig. S1 b). The lipid-S525 interactions result in an increase of hydration near the cation entrance point at the extracellular end of VSD (Z ~8 Å) and a dilation of this region. The solvent accessible surface areas for position 525 are 306 and 226 $Å^2$ for K525S and WT hERG1, respectively
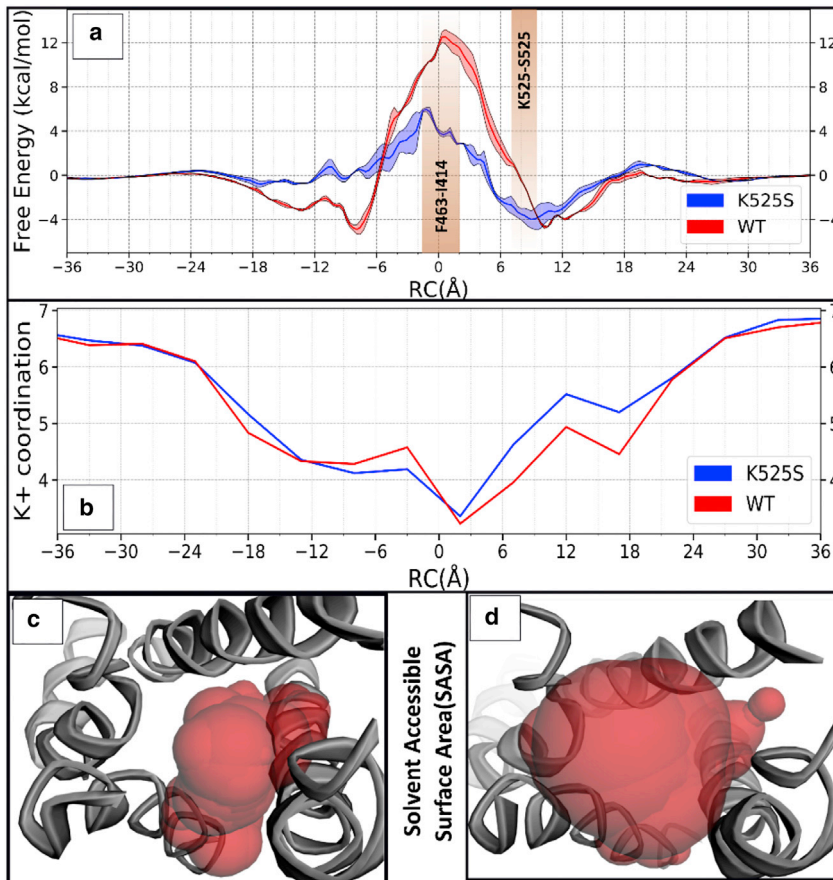
FIGURE 8 The free energy profiles (PMF) of K^+ permeating across the VSD in WT and K525S hERG1 channels, respectively (*a*). Z = 0 Å corresponds to the location of the hydrophobic plug (F463-I414) and shaded areas are standard error of the mean, obtained by using values from calculating PMF three times (see methods for more details). (*b*) The position-dependent water coordination number in the first shell of the permeating cation (K^+). (*c*) Solvent accessibility area (SASA) at the apex of S4 for the WT K525 (SA area: 226 Å), and (*d*) the entry point of a K^+ for the K525S mutant (SA area: 306 Å). SASA is shown as a transparent red-filled volume and calculated for a sphere with a radius of 9 Å centered at K525 or S525. To see this figure in color, go online.

(Fig. 8 *c*). Therefore, the disruption of the intrasubunit interactions in K525S-hERG1 results in the widened and well-hydrated entry region for permeating cation. Therefore, the results of MD and free energy simulations portray a self-consistent mechanism involving the formation of a cation-selective permeation pathway in the VSD of a non-swapped topology channel.

The data from multimicroseconds MD simulations show that the VSD forms wide open crevices while forming and maintaining salt bridges of the open-state hERG1. Previous studies combining cysteine mutagenesis with external pCMBS experiments also showed that S4 residues 522–529 are accessible during depolarization, the open state of the channel (90). The protein-lipid interactions observed in the simulations are in agreement with the published tryptophan scanning mutagenesis, hinting that the S4 residues are exposed to lipids in one or more transient open states of the channel due to the formation of wide crevices (27).

CONCLUSIONS

Here, we experimentally show that the K525S substitution in the voltage sensor of the hERG1 channel opens a robust cation-selective channel with permeation properties similar to the previously reported omega current phenomena. Over-all, the conductance of reported omega currents in voltage-gated channels varies greatly, we found that the K525S nonselective current in hERG is similar to the nonproton omega current reported in *Shaker* (35,97,98), but is smaller than those in Nav channels (2,82).

We find that the presence of the specific chemical moieties in position 525 is a determining factor of the omega current formation (Fig. S5). However, many of the elements required for omega currents are already present in the loosely packed VSD of hERG1. The multimicroseconds-long all-atom MD simulations show the rapid formation of the wide crevices at the extracellular and intracellular sides in WT hERG1 and the S525K closed-state hERG and a subsequent formation of the water wire across the VSD. The free energy simulations reveal two key points: 1) serine substitution stabilizes protein-lipid interactions in position 525, causing increased hydration of the permeation pathway for cations; and 2) the increased hydration of the VSD interior leads to a significant destabilization of the hydrophobic gate formed by F463 and I414 residues, greatly reducing the permeation barrier for cations at the constriction point. Mutation-enhanced hydration and loose packing of the hydrophobic constriction region in hERG1 VSD appeared to be critical structural elements enabling omega current in the K525S hERG1 channel.

SUPPORTING MATERIAL

Supporting material can be found online at https://doi.org/10.1016/j.bpj.2022.10.032.

AUTHOR CONTRIBUTIONS

J.G., J.L.-M., and H.J.D. designed, conducted, and analyzed the experiments. M.K., W.M., V.A.N., M.M., and S.Y.N. designed the simulation studies. M.K., J.G., and D.P.T. drafted the paper with assistance from all co-authors.

ACKNOWLEDGMENTS

DECLARATION OF INTERESTS

The authors declare no competing interests.

REFERENCES

1. Starace, D. M., and F. Bezanilla. 2004. A proton pore in a potassium channel voltage sensor reveals a focused electric field. *Nature.* 427:548–553. https://doi.org/10.1038/nature02270. https://www.ncbi.nlm.nih.gov/pubmed/14765197.

2. Sokolov, S., T. Scheuer, and W. A. Catterall. 2005. Ion permeation through a voltage- sensitive gating pore in brain sodium channels having voltage sensor mutations. *Neuron.* 47:183–189. https://doi.org/10.1016/j.neuron.2005.06.012. https://www.ncbi.nlm.nih.gov/pubmed/16039561.

3. Gamal El-Din, T. M., H. Heldstab, …, N. G. Greeff. 2010. Double gaps along Shaker S4 demonstrate omega currents at three different closed states. *Channels.* 4:93–100. https://www.ncbi.nlm.nih.gov/pubmed/20009570.

4. Smith, P. L., T. Baukrowitz, and G. Yellen. 1996. The inward rectification mechanism of the HERG cardiac potassium channel. *Nature.* 379:833–836. https://doi.org/10.1038/379833a0. https://www.ncbi.nlm.nih.gov/pubmed/8587608.

5. Gutman, G. A., K. G. Chandy, …, P. International Union of. 2003. International Union of Pharmacology. XLI. Compendium of voltage-gated ion channels: potassium channels. *Pharmacol. Rev.* 55:583–586. https://doi.org/10.1124/pr.55.4.9. https://www.ncbi.nlm.nih.gov/pubmed/14657415.

6. Schonherr, R., and S. H. Heinemann. 1996. Molecular determinants for activation and inactivation of HERG, a human inward rectifier potassium channel. *J. Physiol.* 493:635–642. https://doi.org/10.1113/jphysiol.1996.sp021410. https://www.ncbi.nlm.nih.gov/pubmed/8799887.

7. Trudeau, M. C., J. W. Warmke, …, G. A. Robertson. 1995. HERG, a human inward rectifier in the voltage-gated potassium channel family. *Science.* 269:92–95. https://doi.org/10.1126/science.7604285. https://www.ncbi.nlm.nih.gov/pubmed/7604285.

8. Wang, S., S. Liu, …, R. L. Rasmusson. 1997. A quantitative analysis of the activation and inactivation kinetics of HERG expressed in Xenopus oocytes. *J. Physiol.* 502:45–60. https://doi.org/10.1111/j.1469-7793.1997.045bl.x. https://www.ncbi.nlm.nih.gov/pubmed/9234196.

9. Warmke, J. W., and B. Ganetzky. 1994. A family of potassium channel genes related to eag in Drosophila and mammals. *Proc. Natl. Acad. Sci. USA.* 91:3438–3442. https://doi.org/10.1073/pnas.91.8.3438. https://www.ncbi.nlm.nih.gov/pubmed/8159766.

10. Morais Cabral, J. H., A. Lee, …, R. Mackinnon. 1998. Crystal structure and functional analysis of the HERG potassium channel N terminus: a eukaryotic PAS domain. *Cell.* 95:649–655. https://doi.org/10.1016/s0092-8674(00)81635-9. https://www.ncbi.nlm.nih.gov/pubmed/9845367.

11. Bezanilla, F. 2008. How membrane proteins sense voltage. *Nat. Rev. Mol. Cell Biol.* 9:323–332. https://doi.org/10.1038/nrm2376. https://www.ncbi.nlm.nih.gov/pubmed/18354422.

12. Aggarwal, S. K., and R. MacKinnon. 1996. Contribution of the S4 segment to gating charge in the Shaker K+ channel. *Neuron.* 16:1169–1177. https://www.ncbi.nlm.nih.gov/pubmed/8663993.

13. Liman, E. R., P. Hess, …, G. Koren. 1991. Voltage-sensing residues in the S4 region of a mammalian K+ channel. *Nature.* 353:752–756. https://doi.org/10.1038/353752a0. https://www.ncbi.nlm.nih.gov/pubmed/1944534.

14. Seoh, S. A., D. Sigg, …, F. Bezanilla. 1996. Voltage-sensing residues in the S2 and S4 segments of the Shaker K+ channel. *Neuron.* 16:1159–1167. https://doi.org/10.1016/s0896-6273(00)80142-7. https://www.ncbi.nlm.nih.gov/pubmed/8663992.

15. Perozo, E., L. Santacruz-Toloza, …, D. M. Papazian. 1994. S4 mutations alter gating currents of Shaker K channels. *Biophys. J.* 66:345–354. https://doi.org/10.1016/s0006-3495(94)80783-0. https://www.ncbi.nlm.nih.gov/pubmed/8161688.

16. Zhang, M., J. Liu, and G. N. Tseng. 2004. Gating charges in the activation and inactivation processes of the HERG channel. *J. Gen. Physiol.* 124:703–718. https://doi.org/10.1085/jgp.200409119. https://www.ncbi.nlm.nih.gov/pubmed/15545400.

17. Es-Salah-Lamoureux, Z., R. Fougere, …, D. Fedida. 2010. Fluorescence-tracking of activation gating in human ERG channels reveals rapid S4 movement and slow pore opening. *PLoS One.* 5:e10876. https://doi.org/10.1371/journal.pone.0010876. https://www.ncbi.nlm.nih.gov/pubmed/20526358.

18. Piper, D. R., A. Varghese, …, M. Tristani-Firouzi. 2003. Gating currents associated with intramembrane charge displacement in HERG potassium channels. *Proc. Natl. Acad. Sci. USA.* 100:10534–10539. https://doi.org/10.1073/pnas.1832721100. https://www.ncbi.nlm.nih.gov/pubmed/12928493.

19. Subbiah, R. N., C. E. Clarke, …, J. I. Vandenberg. 2004. Molecular basis of slow activation of the human ether-a-go-go related gene potassium channel. *J. Physiol.* 558:417–431. https://doi.org/10.1113/jphysiol.2004.062588. https://www.ncbi.nlm.nih.gov/pubmed/15181157.

20. Zhang, M., J. Liu, …, G. N. Tseng. 2005. Interactions between charged residues in the transmembrane segments of the voltage-sensing domain in the hERG channel. *J. Membr. Biol.* 207:169–181. https://doi.org/10.1007/s00232-005-0812-1.

21. Wang, Z., Y. Dou, …, D. Fedida. 2013. Components of gating charge movement and S4 voltage-sensor exposure during activation of hERG channels. *J. Gen. Physiol.* 141:431–443. https://doi.org/10.1085/jgp.201210942. https://www.ncbi.nlm.nih.gov/pubmed/23478995.

22. Wang, W., and R. MacKinnon. 2017. Cryo-EM structure of the open human ether-a-go-go-related K(+) channel hERG. *Cell.* 169:422–430.e10. https://doi.org/10.1016/j.cell.2017.03.048. https://www.ncbi.nlm.nih.gov/pubmed/28431243.

23. Whicher, J. R., and R. MacKinnon. 2019. Regulation of Eag1 gating by its intracellular domains. *Elife.* 8:e49188.

24. Ramentol, R., M. E. Perez, and H. P. Larsson. 2020. Gating mechanism of hyperpolarization-activated HCN pacemaker channels. *Nat. Commun.* 11:1419. https://doi.org/10.1038/s41467-020-15233-9.

25. Kasimova, M. A., D. Tewari, and B. Chanda. 2019. Helix breaking transition in the S4 of HCN channel is critical for hyperpolarization-dependent gating. *Elife.* 8:e53400.

26. Wang, W., and R. MacKinnon. 2017. Cryo-EM structure of the open human ether-à-go-go-related K+ channel hERG. *Cell.* 169:422–430.e10. https://doi.org/10.1016/j.cell.2017.03.048.

27. Subbiah, R. N., M. Kondo, …, J. I. Vandenberg. 2005. Tryptophan scanning mutagenesis of the HERG K+ channel: the S4 domain is loosely packed and likely to be lipid exposed. *J. Physiol.-London.* 569:367–379. https://doi.org/10.1113/jphysiol.2005.097386.

28. Hong, K. H., and C. Miller. 2000. The lipid-protein interface of a Shaker K+ channel. *J. Gen. Physiol.* 115:51–58. https://doi.org/10.1085/jgp.115.1.51.

29. Monks, S. A., D. J. Needleman, and C. Miller. 1999. Helical structure and packing orientation of the S2 segment in the Shaker K+ channel. *J. Gen. Physiol.* 113:415–423. https://doi.org/10.1085/jgp.113.3.415.

30. Collins, A., H. H. Chuang, …, L. Y. Jan. 1997. Scanning mutagenesis of the putative transmembrane segments of K(ir)2.1, an inward rectifier potassium channel. *Proc Nat. Acad. Sci. USA.* 94:5456–5460. https://doi.org/10.1073/pnas.94.10.5456.

31. Perry, M. D., S. Wong, …, J. I. Vandenberg. 2013. Hydrophobic interactions between the voltage sensor and pore mediate inactivation in Kv11.1 channels. *J. Gen. Physiol.* 142:275–288. https://doi.org/10.1085/jgp.201310975. PMID: 23980196.

32. Khan, H. M., J. Guo, …, S. Y. Noskov. 2021. Refinement of a cryo-EM structure of hERG: bridging structure and function. *Biophys. J.* 120. https://doi.org/10.1016/j.bpj.2021.01.011.

33. Treptow, W., B. Maigret, …, M. Tarek. 2004. Coupled motions between pore and voltage-sensor domains: a model for Shaker B, a voltage-gated potassium channel. *Biophys. J.* 87:2365–2379. https://doi.org/10.1529/biophysj.104.039628.

34. Gosselin-Badaroudine, P., L. Delemotte, …, M. Chahine. 2012. Gating pore currents and the resting state of Nav1.4 voltage sensor domains. *Proc. Natl. Acad. Sci. USA.* 109:19250–19255. https://www.ncbi.nlm.nih.gov/pubmed/23134726.

35. Tombola, F., M. M. Pathak, and E. Y. Isacoff. 2005. Voltage-sensing arginines in a potassium channel permeate and occlude cation-selective pores. *Neuron.* 45:379–388. https://doi.org/10.1016/j.neuron.2004.12.047. https://www.ncbi.nlm.nih.gov/pubmed/15694325.

36. Miceli, F., E. Vargas, …, M. Taglialatela. 2012. Gating currents from Kv7 channels carrying neuronal hyperexcitability mutations in the voltage-sensing domain. *Biophys. J.* 102:1372–1382. https://doi.org/10.1016/j.bpj.2012.02.004.

37. Jurkat-Rott, K., N. Mitrovic, …, F. Lehmann-Horn. 2000. Voltage-sensor sodium channel mutations cause hypokalemic periodic paralysis type 2 by enhanced inactivation and reduced current. *Proc. Natl. Acad. Sci. USA.* 97:9549–9554. https://doi.org/10.1073/pnas.97.17.9549. https://www.ncbi.nlm.nih.gov/pubmed/10944223.

38. Sokolov, S., T. Scheuer, and W. A. Catterall. 2008. Depolarization-activated gating pore current conducted by mutant sodium channels in potassium-sensitive normokalemic periodic paralysis. *Proc. Natl. Acad. Sci. USA.* 105:19980–19985. https://doi.org/10.1073/pnas.0810562105. https://www.ncbi.nlm.nih.gov/pubmed/19052238.

39. Sokolov, S., T. Scheuer, and W. A. Catterall. 2007. Gating pore current in an inherited ion channelopathy. *Nature.* 446:76–78. https://doi.org/10.1038/nature05598. https://www.ncbi.nlm.nih.gov/pubmed/17330043.

40. Struyk, A. F., and S. C. Cannon. 2007. A Na+ channel mutation linked to hypokalemic periodic paralysis exposes a proton-selective gating pore. *J. Gen. Physiol.* 130:11–20. https://doi.org/10.1085/jgp.200709755. https://www.ncbi.nlm.nih.gov/pubmed/17591984.

41. Matthews, E., R. Labrum, …, M. G. Hanna. 2009. Voltage sensor charge loss accounts for most cases of hypokalemic periodic paralysis. *Neurology.* 72:1544–1547. https://doi.org/10.1212/01.wnl.0000342387.65477.46. https://www.ncbi.nlm.nih.gov/pubmed/19118277.

42. Bulman, D. E., K. A. Scoggan, …, G. C. Ebers. 1999. A novel sodium channel mutation in a family with hypokalemic periodic paralysis. *Neurology.* 53:1932–1936. https://doi.org/10.1212/wnl.53.9.1932. https://www.ncbi.nlm.nih.gov/pubmed/10599760.

43. Cheng, Y. M., C. M. Hull, …, T. W. Claydon. 2013. Functional interactions of voltage sensor charges with an S2 hydrophobic plug in hERG channels. *J. Gen. Physiol.* 142:289–303. https://doi.org/10.1085/jgp.201310992. https://www.ncbi.nlm.nih.gov/pubmed/23980197.

44. Lees-Miller, J. P., J. Q. Guo, …, H. J. Duff. 2015. Ivabradine prolongs phase 3 of cardiac repolarization and blocks the hERG1 (KCNH2) current over a concentration-range overlapping with that required to block HCN4. *J. Mol. Cell. Cardiol.* 85:71–78. https://doi.org/10.1016/j.yjmcc.2015.05.009.

45. Wang, Y., J. Guo, …, S. Y. Noskov. 2016. Role of the pH in state-dependent blockade of hERG currents. *Sci. Rep.* 6:32536. https://doi.org/10.1038/srep32536.

46. Lees-Miller, J. P., J. Guo, …, H. J. Duff. 2015. Ivabradine prolongs phase 3 of cardiac repolarization and blocks the hERG1 (KCNH2) current over a concentration-range overlapping with that required to block HCN4. *J. Mol. Cell. Cardiol.* 85:71–78. https://doi.org/10.1016/j.yjmcc.2015.05.009. https://www.ncbi.nlm.nih.gov/pubmed/25986146.

47. Perissinotti, L., J. Guo, …, H. J. Duff. 2019. The pore-lipid interface: role of amino-acid determinants of lipophilic access by ivabradine to the hERG1 pore domain. *Mol. Pharmacol.* 96:259–271. https://doi.org/10.1124/mol.118.115642. https://www.ncbi.nlm.nih.gov/pubmed/31182542.

48. Huang, J., S. Rauscher, …, A. D. MacKerell, Jr. 2017. CHARMM36m: an improved force field for folded and intrinsically disordered proteins. *Nat. Methods.* 14:71–73. https://doi.org/10.1038/nmeth.4067. https://www.ncbi.nlm.nih.gov/pubmed/27819658.

49. Shaw, D. E., J. P. Grossman, …, A. Forte. 2014. Anton 2: Raising the Bar for Performance and Programmability in a Special-Purpose Molecular Dynamics Supercomputer. IEEE Press, pp. 41–53.. https://doi.org/10.1109/SC.2014.9.

50. Lippert, R. A., C. Predescu, …, D. E. Shaw. 2013. Accurate and efficient integration for molecular dynamics simulations at constant temperature and pressure. *J. Chem. Phys.* 139:164106. https://doi.org/10.1063/1.4825247. https://www.ncbi.nlm.nih.gov/pubmed/24182003.

51. Shaw, D. E., J. P. Grossman, …, C. Young. 2014. Anton 2: raising the bar for performance and programmability in a special-purpose molecular dynamics supercomputer. *Int Conf High Perfor* 41–53.

52. Tuckerman, M., B. J. Berne, and G. J. Martyna. 1992. Reversible multiple time scale molecular dynamics. *J. Chem. Phys.* 97:1990–2001.

53. Shan, Y. B., J. L. Klepeis, …, D. E. Shaw. 2005. Gaussian split Ewald: a fast Ewald mesh method for molecular simulation. *J. Chem. Phys.* 122. Artn 054101. https://doi.org/10.1063/1.1839571.

54. Klauda, J. B., R. M. Venable, …, R. W. Pastor. 2010. Update of the CHARMM all-atom additive force field for lipids: validation on six lipid types. *J. Phys. Chem. B.* 114:7830–7843. https://doi.org/10.1021/jp101759q. https://www.ncbi.nlm.nih.gov/pubmed/20496934.

55. Klauda, J. B., V. Monje, …, W. Im. 2012. Improving the CHARMM force field for polyunsaturated fatty acid chains. *J. Phys. Chem. B.* 116:9424–9431. https://doi.org/10.1021/jp304056p. https://www.ncbi.nlm.nih.gov/pubmed/22697583.

56. Jorgensen, W. L., J. Chandrasekhar, …, M. L. Klein. 1983. Comparison of simple potential functions for simulating liquid water. *J. Chem. Phys.* 79:926–935. https://doi.org/10.1063/1.445869.

57. Noskov, S. Y., and B. Roux. 2008. Control of ion selectivity in LeuT: two Na+ binding sites with two different mechanisms. *J. Mol. Biol.* 377:804–818. https://doi.org/10.1016/j.jmb.2008.01.015.

58. Phillips, J. C., R. Braun, …, K. Schulten. 2005. Scalable molecular dynamics with NAMD. *J. Comput. Chem.* 26:1781–1802. https://doi.org/10.1002/jcc.20289. https://www.ncbi.nlm.nih.gov/pubmed/16222654.

59. William Humphrey, A. D., and K. Schulten. 1996. VMD: visual molecular dynamics. *J. Mol. Graph.* 14:33–38.

60. The PyMOL Molecular Graphics System, V. S., LLC.

61. Dai, G., T. K. Aman, ..., W. N. Zagotta. 2019. The HCN channel voltage sensor undergoes a large downward motion during hyperpolarization. *Nat. Struct. Mol. Biol.* 26:686–694. https://doi.org/10.1038/s41594-019-0259-1. https://www.ncbi.nlm.nih.gov/pubmed/31285608.

62. Whicher, J. R., and R. MacKinnon. 2016. Structure of the voltage-gated K(+) channel Eag1 reveals an alternative voltage sensing mechanism. *Science.* 353:664–669. https://doi.org/10.1126/science.aaf8070. https://www.ncbi.nlm.nih.gov/pubmed/27516594.

63. Kopp, J., and T. Schwede. 2004. The SWISS-MODEL Repository of annotated three-dimensional protein structure homology models. *Nucleic Acids Res.* 32:D230–D234. https://doi.org/10.1093/nar/gkh008. https://www.ncbi.nlm.nih.gov/pubmed/14681401.

64. Jo, S., T. Kim, ..., W. Im. 2008. CHARMM-GUI: a web-based graphical user interface for CHARMM. *J. Comput. Chem.* 29:1859–1865. https://doi.org/10.1002/jcc.20945. https://www.ncbi.nlm.nih.gov/pubmed/18351591.

65. Campos, F. V., B. Chanda, ..., F. Bezanilla. 2007. Two atomic constraints unambiguously position the S4 segment relative to S1 and S2 segments in the closed state of Shaker K channel. *Proc. Natl. Acad. Sci. USA.* 104:7904–7909. https://doi.org/10.1073/pnas.0702638104. https://www.ncbi.nlm.nih.gov/pubmed/17470814.

66. Lewis, A., V. Jogini, ..., B. Roux. 2008. Atomic constraints between the voltage sensor and the pore domain in a voltage-gated K+ channel of known structure. *J. Gen. Physiol.* 131:549–561. https://doi.org/10.1085/jgp.200809962. https://www.ncbi.nlm.nih.gov/pubmed/18504314.

67. Khalili-Araghi, F., V. Jogini, ..., K. Schulten. 2010. Calculation of the gating charge for the Kv1.2 voltage-activated potassium channel. *Biophys. J.* 98:2189–2198. https://doi.org/10.1016/j.bpj.2010.02.056. https://www.ncbi.nlm.nih.gov/pubmed/20483327.

68. Roux, B. 2008. The membrane potential and its representation by a constant electric field in computer simulations. *Biophys. J.* 95:4205–4216. https://doi.org/10.1529/biophysj.108.136499. https://www.ncbi.nlm.nih.gov/pubmed/18641071.

69. Sunhwan Jo, J. B. L., J. B. Klauda, and I. Wonpil. 2009. CHARMM-GUI membrane builder for mixed bilayers and its application to yeast membranes. *Biophys. J.* 97:50–58.

70. Yuji Sugita, Y. O. 1999. Replica-exchange molecular dynamics method for protein folding. *Chem. Phys. Lett.* 314:141–151.

71. Ngo, V., H. Li, ..., S. Noskov. 2021. Polarization effects in water-mediated selective cation transport across a narrow transmembrane channel. *J. Chem. Theor. Comput.* https://doi.org/10.1021/acs.jctc.0c00968.

72. Allen, T. W., O. S. Andersen, and B. Roux. 2006. Ion permeation through a narrow channel: using gramicidin to ascertain all-atom molecular dynamics potential of mean force methodology and biomolecular force fields. *Biophys. J.* 90:3447–3468. https://doi.org/10.1529/biophysj.105.077073.

73. Grossfield, A. 2013. WHAM: the weighted histogram analysis method, version 2.0. 9. membrane.urmc.rochester.edu/content/wham.

74. Jurcik, A., D. Bednar, ..., B. Kozlikova. 2018. CAVER Analyst 2.0: analysis and visualization of channels and tunnels in protein structures and molecular dynamics trajectories. *Bioinformatics.* 34:3586–3588. https://doi.org/10.1093/bioinformatics/bty386.

75. Petrek, M., M. Otyepka, ..., J. Damborsky. 2006. CAVER: a new tool to explore routes from protein clefts, pockets and cavities. *BMC Bioinf.* 7:Artn 316.

76. Whitfield, T. W., S. Varma, ..., B. Roux. 2007. A theoretical study of aqueous solvation of K comparing ab initio, polarizable, and fixed-charge models. *J. Chem. Theor. Comput.* 3:2068–2082. https://doi.org/10.1021/ct700172b. https://www.ncbi.nlm.nih.gov/pubmed/21785577.

77. Tian, W., C. Chen, ..., J. Liang. 2018. CASTp 3.0: computed atlas of surface topography of proteins. *Nucleic Acids Res.* 46:W363–W367. https://doi.org/10.1093/nar/gky473. https://www.ncbi.nlm.nih.gov/pubmed/29860391.

78. Saxena, P., E. M. Zangerl-Plessl, ..., A. Stary-Weinzinger. 2016. New potential binding determinant for hERG channel inhibitors. *Sci. Rep.* 6:24182. https://doi.org/10.1038/srep24182. https://www.ncbi.nlm.nih.gov/pubmed/27067805.

79. Weerapura, M., S. Nattel, ..., T. Hebert. 2000. State-dependent barium block of wild-type and inactivation-deficient HERG channels in Xenopus oocytes. *J. Physiol.* 526:265–278. https://doi.org/10.1111/j.1469-7793.2000.t01-1-00265.x. https://www.ncbi.nlm.nih.gov/pubmed/10896755.

80. Lees-Miller, J. P., Y. J. Duan, ..., H. J. Duff. 2000. Molecular determinant of high-affinity dofetilide binding to HERG1 expressed in Xenopus oocytes: involvement of S6 sites. *Mol. Pharmacol.* 57:367–374.

81. Guo, J., Y. M. Cheng, ..., H. J. Duff. 2015. NS1643 interacts around L529 of hERG to alter voltage sensor movement on the path to activation. *Biophys. J.* 108:1400–1413. https://doi.org/10.1016/j.bpj.2014.12.055. https://www.ncbi.nlm.nih.gov/pubmed/25809253.

82. Sokolov, S., T. Scheuer, and W. A. Catterall. 2010. Ion permeation and block of the gating pore in the voltage sensor of NaV1.4 channels with hypokalemic periodic paralysis mutations. *J. Gen. Physiol.* 136:225–236. https://doi.org/10.1085/jgp.201010414. https://www.ncbi.nlm.nih.gov/pubmed/20660662.

83. Klassen, T. L., A. N. Spencer, and W. J. Gallin. 2008. A naturally occurring omega current in a Kv3 family potassium channel from a platyhelminth. *BMC Neurosci.* 9:52. https://doi.org/10.1186/1471-2202-9-52. https://www.ncbi.nlm.nih.gov/pubmed/18565223.

84. Shi, Y. P., Y. M. Cheng, ..., T. W. Claydon. 2014. External protons destabilize the activated voltage sensor in hERG channels. *Eur. Biophys. J.* 43:59–69. https://doi.org/10.1007/s00249-013-0940-y. https://www.ncbi.nlm.nih.gov/pubmed/24362825.

85. Van Slyke, A. C., S. Rezazadeh, ..., T. W. Claydon. 2010. Mutations within the S4-S5 linker alter voltage sensor constraints in hERG K+ channels. *Biophys. J.* 99:2841–2852. https://doi.org/10.1016/j.bpj.2010.08.030. https://www.ncbi.nlm.nih.gov/pubmed/21044581.

86. Piper, D. R., J. Rupp, ..., M. Tristani-Firouzi. 2008. Cooperative interactions between R531 and acidic residues in the voltage sensing module of hERG1 channels. *Cell. Physiol. Biochem.* 21:37–46. https://doi.org/10.1159/000113745. https://www.ncbi.nlm.nih.gov/pubmed/18209470.

87. Liu, J., M. Zhang, ..., G. N. Tseng. 2003. Negative charges in the transmembrane domains of the HERG K channel are involved in the activation- and deactivation-gating processes. *J. Gen. Physiol.* 121:599–614. https://doi.org/10.1085/jgp.200308788. https://www.ncbi.nlm.nih.gov/pubmed/12771194.

88. Shi, Y. P., S. Thouta, ..., T. W. Claydon. 2019. Extracellular protons accelerate hERG channel deactivation by destabilizing voltage sensor relaxation. *J. Gen. Physiol.* 151:231–246. https://doi.org/10.1085/jgp.201812137. https://www.ncbi.nlm.nih.gov/pubmed/30530765.

89. Tseng, G. N., and H. R. Guy. 2005. Structure-function Studies of the Outer Mouth and Voltage Sensor Domain of hERG. *Novartis Found. Symp.* 266:19, 35-45. https://www.ncbi.nlm.nih.gov/pubmed/16050260.

90. Elliott, D. J., N. Y. Dondas, ..., A. Sivaprasadarao. 2009. Movement of the S4 segment in the hERG potassium channel during membrane depolarization. *Mol. Membr. Biol.* 26:435–447. https://doi.org/10.3109/09687680903321081.

91. Fernandez, D., A. Ghanta, ..., M. C. Sanguinetti. 2005. Molecular mapping of a site for Cd2+-induced modification of human ether-a-go-go-related gene (hERG) channel activation. *J. Physiol.* 567:737–755. https://doi.org/10.1113/jphysiol.2005.089094. https://www.ncbi.nlm.nih.gov/pubmed/15975984.

92. Dou, Y., L. C. Macdonald, ..., D. Fedida. 2017. The fast component of hERG gating charge: an interaction between D411 in the S1 and S4 residues. *Biophys. J.* 113:1979–1991. https://doi.org/10.1016/j.bpj.2017.09.004. https://www.ncbi.nlm.nih.gov/pubmed/29117522.

93. Lacroix, J. J., and F. Bezanilla. 2011. Control of a final gating charge transition by a hydrophobic residue in the S2 segment of a K+ channel voltage sensor. *Proc. Natl. Acad. Sci. USA.* 108:6444–6449. https://doi.org/10.1073/pnas.1103397108. https://www.ncbi.nlm.nih.gov/pubmed/21464282.

94. Qiu, F., A. Chamberlin, ..., H. P. Larsson. 2016. Molecular mechanism of Zn2+ inhibition of a voltage-gated proton channel. *Proc. Natl. Acad. Sci. USA.* 113:E5962–E5971. https://doi.org/10.1073/pnas.1604082113. https://www.ncbi.nlm.nih.gov/pubmed/27647906.

95. Cherny, V. V., B. Musset, …, T. E. DeCoursey. 2020. Engineered high-affinity zinc binding site reveals gating configurations of a human proton channel. *J. Gen. Physiol.* 152. https://doi.org/10.1085/jgp.202012664. https://www.ncbi.nlm.nih.gov/pubmed/32902579.

96. Roux, B., T. Allen, …, W. Im. 2004. Theoretical and computational models of biological ion channels. *Q. Rev. Biophys.* 37:15–103. https://doi.org/10.1017/S0033583504003968.

97. Gamal, E. T. M., H. Heldstab, …, N. G. Greeff. 2010. Double gaps along Shaker S4 demonstrate omega currents at three different closed states. *Channels.* 4:93–100.

98. Tombola, F., M. M. Pathak, and E. Y. Isacoff. 2005. Voltage-sensing arginines in a potassium channel permeate and occlude cation-selective pores. *Neuron.* 45:379–388. https://doi.org/10.1016/j.neuron.2004.12.047. PMID: 15694325.